HHS Public Access

Author manuscript

ACS Appl Mater Interfaces. Author manuscript; available in PMC 2019 December 26.

Published in final edited form as:

ACS Appl Mater Interfaces. 2018 December 26; 10(51): 44267–44278. doi:10.1021/acsami.8b17264.

Capsule-Integrated Polypeptide Multilayer Films for Effective pH-Responsive Multiple Drug Co-Delivery

Shichao Zhang[†], **Malcolm Xing**[‡], and **Bingyun Li**[*,†]

[†]Department of Orthopaedics, School of Medicine, West Virginia University, Morgantown, West Virginia 26506, United States

[‡]Department of Mechanical Engineering, University of Manitoba, and The Children's Hospital Research Institute of Manitoba, Winnipeg, Manitoba R3E 3P4, Canada

Abstract

Many applications using drug-carrying biomedical materials require on-demand, localized delivery of multiple therapeutic agents in precisely controlled and patient-specific time sequences, especially after assembly of the delivery vehicles; however, creating such materials has proven extremely challenging. Here, we report a novel strategy to create polypeptide multilayer films integrated with capsules as vehicles for co-delivery of multiple drugs using layer-by-layer self-assembly technology. Our approach allows the multilayered polypeptide nanofilms and preimpregnated capsules to assemble into innovative biomedical materials with high and controllable loading of multiple drugs at any time postpreparation and to achieve pH-responsive and sustained release. The resulting capsule-integrated polypeptide multilayer films effectively co-deliver various drugs with very different properties, including proteins (e.g., growth factors) and nanoparticles, achieving bovine serum albumin loading of 80 μg cm^{-2} and release of 2 weeks, and histone loading of 100 μg cm^{-2} and release of 6 weeks; which also enable *Staphylococcus aureus* killing efficacy of 83% while maintaining osteoblast viability of >85% with silver nanoparticle delivery; and >5-fold cell adhesion and proliferation capability with live cell percentage of >90% via human recombinant bone morphogenetic protein 2 delivery. The successful development of such fascinating materials can not only function as advanced nanocoatings to reduce two major complications of orthopedic bone injuries (i.e., infection and delayed bone regeneration) but also provide new insights into the design and development of multifunctional materials for various other biomedical applications.

[*]**Corresponding Author** bili@hsc.wvu.edu. Tel: 304-293-1075. Fax: 304-293-7070.

Author Contributions

The manuscript was written through contributions of all authors. All authors have given approval to the final version of the manuscript.

ASSOCIATED CONTENT

Supporting Information

The Supporting Information is available free of charge on the ACS Publications website at DOI: 10.1021/acsami.8b17264.

pH values of tissue samples around infected and uninfected rat femurs in an open fracture rat model (Figure S1); growth profiles and stability of PL/PG multilayer films fabricated from various solutions (Figure S2); thickness of the capsule-integrated multilayer films after immersing the films in PBS for various times (Figure S3); SEM images of the capsule-integrated films before and after PBS immersion for 5 days (Figure S4); polypeptide multilayer films of L5/C^{G}/L8/C$^{L\text{-}FITC}$/L8 loaded with Alexa Fluor 647-conjugated BSA for different incubation times (Figure S5); cumulative release profiles of proteins from PL/PG multilayer films with and without capsule^{PL} or capsule^{PG} in SBF (Figure S6); and cumulative release profiles of AgNPs and rhBMP-2 from the L5/C^{G}/L8/C^{L}/L8 films (Figure S7) (PDF)

Graphical Abstract

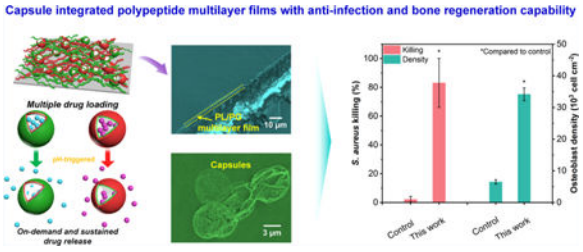

Keywords

layer-by-layer self-assembly; polypeptides; multilayer films; capsules; drug delivery

1. INTRODUCTION

Biomedical implants, as a major component of modern medicine used to substitute missing structure or function in the human body, play a critical role in various clinical applications ranging from tissue repair and reconstruction, bone fracture fixation, hip and knee replacement, and electronic sensory or monitoring to organ transplantation.[1–4] However, implant-associated infection and delayed tissue regeneration are two major clinical complications, in particular for orthopedic implants, and can lead to poor functional outcome, implant failure, additional surgery, and even death.[5–7] To reduce these two complications, the ideal implants should be designed to inhibit bacterial adhesion and colonization and to induce appropriate cellular responses to promote osseointegration without sacrificing the required structural and physicochemical properties and functions.[8,9] Due to its integrated features of cost efficiency, localized release capacity, and ease of large-scale synthesis, surface modification has been considered as one of the most promising strategies to develop drug-delivery materials at the implant/ tissue interface to reduce postoperative infections and to promote wound healing.[10–13] However, the generation of clinical nanomaterials with the capability to deliver drug molecules at the right place and according to patients' needs has been a major challenge and has attracted extensive attention with the rapid development of nanotechnology.

Because of its integrated properties of flexible choice of assembly components, precise control of assembly structure/ properties, and ease of processing on substrates (regardless of size and shape), layer-by-layer (LbL) self-assembly has been known as a highly versatile and facile nanomaterial assembly technique for modifying implants using drug-delivery materials with controlled structures and functions.[14–18] To date, a series of LbL-assembled drug-delivery materials in the form of multilayer films and capsules have been prepared from polyelectrolytes, amphiphilic polymers, hydrogels, micelles, etc.[19–26] Despite the localized and enhanced drug delivery, some drawbacks still remain for these assemblies. For instance, most of these multilayer films carry only a single cargo or have limited loading capacity, in which the drug is assembled as film components; they are still far from satisfactory for most situations in which more than one therapeutic agent is needed.[18,27–30] To enhance drug-loading capacity, hollow capsules have been designed and engineered via

LbL self-assembly of shells on sacrificial templates, however, most of them barely meet the requirements for clinical application due to limited structural controllability (like incompleteness and aggregation), weak mechanical properties (easy to break during implantation), and uncontrolled and unsustained release (burst release).[31,32] Although some multidrug delivery vehicles have been prepared and showed enhanced delivery capability, they loaded drugs during the vehicle assembly process leading to loss of drug bioactivity, limited drug variety (especially for drugs of different properties), and heavy burden on drug storage in vehicles.[33–36] Therefore, creating a strategy to develop delivery vehicles that can achieve on-demand and localized release of multiple drugs in precisely controlled, patient-specific time sequences is still an ongoing challenge. Recently, polypeptide multilayer films that can co-deliver gentamicin and bovine serum albumin (BSA) were first prepared in our group and exhibited an enhanced multidrug loading capacity owing to our unique structural design.[22] This work provided an innovative preparation concept for drug delivery vehicles; however, three challenges still remain: (i) only two model drugs of gentamicin and BSA were used for proof of concept without the capability to resolve the two major complications of implant-associated infection and delayed tissue regeneration, especially, no in vitro or in vivo anti-infection and bone regeneration studies were conducted, (ii) the resultant films had burst release of drugs and no means of controlling the burst release were examined, and (iii) the loaded gentamicin may lead to antibiotic resistance, whereas BSA cannot function as a therapeutic agent for bone regeneration.

Here, we demonstrate a novel strategy for creating capsule-integrated polypeptide films as vehicles to deliver multiple drugs with very different properties (e.g., opposite charges, diverse monomers of molecule/particle) in postpreparation loading and pH-responsive and sustained release manner for preventing implant-associated infections and promoting bone regeneration. Microcapsules impregnated with polyelectrolytes function as primary delivery vehicles with controllable drug binding capability; these microcapsules were designed and evaluated in terms of morphology, structure, and delivery capacity. Moreover, the capsule-integrated film vehicles were obtained by optimizing the loading of impregnated polyelectrolytes in capsules and capsule density in polypeptide multilayer films. In addition, the loading capacities and release profiles of four different drugs (BSA, calf thymus histone H1, silver nanoparticles or AgNPs, and human recombinant bone morphogenetic protein 2 or rhBMP-2), in vivo mechanical properties, in vitro anti-infection capability against *Staphylococcus aureus*, and in vitro bone regeneration capability of our resultant delivery vehicles were conducted to demonstrate the robust application performance resulting from sustained and precisely controlled multidrug delivery in patient-specific time sequences, to resolve the two major complications (i.e., infection and delayed healing) of orthopedic bone injuries.

2. MATERIALS AND METHODS

2.1. Reagents and Materials.

Poly-L-lysine hydrobromide (PL, M_w 150–300 kDa), poly-L-glutamic acid sodium salt (PG, M_w 50–100 kDa), PL labeled with fluorescein isothiocyanate (PL-FITC), sodium hydroxide (≥97.0%), sodium chloride (≥99.5%), tris-(hydroxymethyl)aminomethane (≥99.8%),

glutaraldehyde (GA), rhBMP-2, and rhBMP-2 enzyme-linked immunosorbent assay (ELISA) kit were obtained from Sigma-Aldrich (St. Louis, MO). Simulated body fluid (SBF) was prepared by dissolving reagent-grade salts in deionized water and had a composition of 142.0 mM Na^+, 5.0 mM K^+, 1.5 mM Mg^{2+}, 2.5 mM Ca^{2+}, 4.2 mM HCO_3^-, 147.8 mM Cl^-, 1.0 mM HPO_4^{2-}, and 0.5 mM SO_4^{2-}. Alexa Fluor 647-conjugated BSA, Alexa Fluor 488-conjugated histone H1 from calf thymus, disodium ethylenediaminetetraacetic acid (EDTA), and 0.25% trypsin/2.21 mM EDTA solution were purchased from Thermo Fisher Scientific (Fair Lawn, NJ). Dulbecco's modified Eagle's medium/nutrient mixture F-12 (DMEM/F-12) and penicillin/streptomycin (P/S) were obtained from Life Technologies (Grand Island, NY). Fetal bovine serum (FBS) and Dulbecco's phosphate-buffered saline (PBS, pH 7.0) were purchased from Corning (Manassas, VA). Tryptic soy broth (TSB) was obtained from Becton Dickinson (Sparks, MD). AgNPs (diameter of ~10 nm) capped with poly(vinylpyrrolidone) (PVP) were obtained from nanoComposix, Inc. (San Diego, CA). Calcium carbonate ($CaCO_3$) particles were purchased from PlasmaChem GmbH (Rudower Chaussee, Berlin, Germany). Stainless steel Kirschner wires (K-wires) were purchased from Smith & Nephew, Inc. (Memphis, TN). Quartz microscope slides (76.2 × 50.8 mm^2) were bought from Electron Microscopy Sciences (Hatfield, PA) and cleaned and cut into 10 × 25 mm^2 for further use. N-type (100) silicon wafers were supplied by Montco Silicon Technologies Inc. (Spring City, PA) and cleaved into 10 × 25 mm^2 rectangles for further use.

2.2. LbL Self-Assembly of Multilayer Nanofilms, Microcapsules, and Capsule-Integrated Polypeptide Multilayer Films.

Polypeptide multilayer films were prepared using a dipping machine (Riegler and Kirstein GmbH, Berlin, Germany). In brief, the precleaned substrates (i.e., quartz slides, steel disks, silica wafers, and K-wires) were clamped on the dipping heads and immersed in PL solution (positively charged) for 20 min, then rinsed with tris buffer solution for 3 min, and dried with air. Next, the samples were coated using PG solution (negatively charged) with similar dipping, rinsing, and drying processes. These two coating processes were referred to as one coating cycle for one bilayer construction and can be repeated to deposit a multilayer film with a well-defined structure and thickness.

To construct microcapsules for drug delivery, the polyelectrolytes (i.e., PL or PG) were impregnated into $CaCO_3$ particles via immersing them into 2 mg mL^{-1} PL or PG solution for 30 min under vacuum pressure (3 Torr). The samples underwent a centrifugation to remove the supernatant and were dried in a vacuum oven (380 Torr) at 60 °C overnight. Polypeptides (i.e., PL and PG) were then alternatively used to construct the multilayer shells on these preimpregnated particles using LbL self-assembly to form shelled $CaCO_3$ particles, in a similar manner as described above for coating on conventional substrates, however, in this case, a centrifugation (3000 rpm for 1 min) step was added between the two coating processes to make the coating processes on microparticles feasible. After that the shelled $CaCO_3$ particles were subjected to cross-linking by incubating them in a 25% GA solution for 3 h to stabilize the multilayer shell. To form microcapsules, these shelled particles were incubated in 0.1 M EDTA solution for 1 h, followed by centrifugation, and removal of supernatants to dissolve the $CaCO_3$ templates. Here, PL- and PG-impregnated $CaCO_3$

particles and their resultant capsules were designated as $CaCO_3^{PL}$, $CaCO_3^{PG}$, $capsule^{PL}$, and $capsule^{PG}$, respectively.

The construction of capsule-integrated polypeptide multilayer films for multidrug delivery was carried out by combining the LbL self-assembly processes of multilayer nanofilms and microcapsules. The typical procedure is shown in Scheme 1: (1) self-assembly of $(PL/PG)_x$ multilayer nanofilms; (2) deposition of $CaCO_3^{PG}$ particles; (3) self-assembly of $PG/(PL/PG)_y$ multilayer nanofilms; (4) deposition of $CaCO_3^{PL}$ particles; (5) self-assembly of $PG/(PL/PG)_z$ multilayer nanofilms; and (6) formation of capsule-integrated multilayer films by dissolving $CaCO_3$ templates. In this work, the multilayer shells for $CaCO_3^{PL}$ and $CaCO_3^{PG}$ particles were optimized as $(PL/PG)_{3.5}$ films. The depositions of $CaCO_3^{PL}$ or $CaCO_3^{PG}$ particles were achieved by dipping the nanofilms into 2 mL suspensions of shelled particles (particle density of 6×10 mL^{-1}) for a specific duration. The final capsule-integrated polypeptide multilayer films were referred to as $(PL/PG)_x/capsule^{PG}/PG/(PL/PG)_y/capsule^{PL}/PG/(PL/PG)_z$, which was further simplified as $L_x/C^G/L_y/C^L/L_z$ where L represents PL/PG layers, C^G and C^L represent PG and PL-impregnated capsules, respectively, and x, y, and z are the numbers of PL/PG bilayers.

2.3. Drug Loading and Release.

To load the drug models of fluorescently labeled BSA and histone, the multilayer films (coated on 2×2 cm^2 quartz slides) were incubated in 1 mg mL^{-1} of BSA or histone solution (pH 7.4, PBS buffered) for various times. To load AgNP, the capsule-integrated multilayer films were immersed into 0.1 mg mL^{-1} of AgNP suspension. rhBMP-2 loading was conducted by incubating the capsule-integrated films in 4 μg mL^{-1} of rhBMP-2 solution (pH 7.4, PBS buffered). After incubating for a predetermined time period, the samples were washed briefly in PBS to remove the loosely attached drug molecules or nanoparticles. The loading of fluorescence-labeled drugs was confirmed using confocal laser scanning microscopy (CLSM, LSM 510, Zeiss, Thornwood, NY), and their quantitative loading and release were measured using a hybrid multimode microplate reader (Synergy H4, Winooski, VT) as previously reported.[9,37] In brief, the drug-loaded samples were sonicated in PBS, and the amounts of encapsulated drugs or fluorescently labeled vehicles in the samples were quantitatively determined. The drug-loading and encapsulation rate were calculated using the following equations: (i) drug-loading rate = the amount of drug encapsulated in the delivery vehicles/the total amount of delivery vehicles × 100% and (ii) encapsulation efficiency = the amount of drug encapsulated in the delivery vehicles/the amount of drug in the loading solution × 100%. The drug release measurements were conducted by incubating the drug-loaded delivery vehicles in 2 mL of PBS or SBF (pH = 7.4) placed in a 37 °C water bath on a rocker. At predetermined time periods, 400 μL of medium was taken to measure the release of drugs, and 400 μL fresh PBS was added to keep the medium volume constant; the cumulative drug release was calculated.

2.4. Cell Culture, Adhesion, and Proliferation.

A human osteoblast cell line CRL-11372 was supplied by American Type Cell Culture (Manassas, VA) and cultured in 1:1 DMEM/F-12 medium supplemented with 10% FBS and 1% P/S in a T75 cell culture flask and incubated at 37 °C in a 5% CO_2 atmosphere.

Osteoblast cells were detached from the T75 flask using trypsin-EDTA solution and added (cell density of 10 000 cell cm^{-2}) into 24-well culture plates, in which the coated and uncoated sterile quartz slides were placed. The culture medium was replaced every other day. A clinical isolate of *S. aureus* (SA 1004) was obtained from Ruby Memorial Hospital (Morgantown, WV) and stocked on sheep blood agar plates at 4 °C. Before using, *S. aureus* was first cultured in TSB for 16 h at 37 °C and then diluted with fresh TSB and incubated at 37 °C for an additional 3 h to achieve log-phase growth. Different molar concentrations of AgNPs and coated substrates with/without AgNP loading were added to 1 mL of inoculum with a concentration of 1.0×10^5 colony forming units per milliliter (CFU mL^{-1}) and incubated for 24 h at 37 °C.

2.5. Characterization.

The morphologies of $CaCO_3$ particles, microcapsules, PL/PG nanofilms, and capsule-integrated films were characterized using S-4700 scanning electron microscope (SEM, Hitachi Ltd., Japan) with an acceleration voltage of 5 kV after being coated with gold for 100 s and NanoScope atomic force microscopy (AFM, PicoSPM II, Tempe, AZ) operating in a tapping mode. The thickness of multilayer films was examined using UV-vis spectrometry (BioMate 3S, Thermo Electron Co., NY) and ellipsometry (M- 2000, JA Woollam Co., Lincoln, NE). The water contact angle data (3 μL) were collected using macrophotography of iPhone 7 plus and analyzed by Adobe Photoshop CS6 image analysis software. The size distribution of AgNPs was collected with a Malvern NanoSight NS300 instrument using NTA Nanosight 3.2 software (Malvern Instruments, Westborough, MA), whereas their ζ potential was measured using a Malvern Zetasizer Nano Z using Zetasizer software (Malvern Instruments). To determine the *S. aureus* killing efficacy, the samples from a 24-well culture plate were diluted (10^{-4}, 10^{-5}, and 10^{-6}) in sterile PBS after various treatments, plated on 5% sheep blood agar plates, and incubated for 24 h at 37 °C. The numbers of CFUs were quantified, and the killing efficacy was calculated by dividing the difference between the number of CFUs in the control and the number of CFUs in the treated samples with the number of CFUs in the control and then multiplying by 100. Osteoblast cell adhesion and proliferation were determined after detaching and counted using a hemocytometer under a light microscope. Briefly, after culturing for a specific duration, the substrates were removed from culture plates and rinsed with PBS three times. Then, a typical trypsinization procedure, followed by centrifugation, was introduced to detach cells on the substrates. After resuspending in PBS, the number of cells was counted using a hemocytometer. Furthermore, the osteoblast viability assay was carried out using trypan blue to count the number of viable cells. All data were presented as means ± standard deviations. Comparisons between two groups were conducted using the Student's *t*-test, whereas comparisons between three groups or more were conducted with one-way analysis of variance followed by Tukey's honestly significant difference test. *P*-value < 0.05 was considered statistically significant.

3. RESULTS AND DISCUSSION

3.1. Structural Design and Analysis of Capsule- Integrated Multilayer Films.

To create a drug-delivery system that can achieve high loading and on-demand and sustained release of desired drugs requires a sophisticated structural design of delivery vehicles.[38,39] We constructed our multidrug delivery vehicles via a hierarchical nano/microlevel design based on three criteria: (l) the environment-responsive microcapsules must be assembled to function as vehicles for multiple drugs of very different properties, (2) different capsules in the constructed delivery system must be highly organized to achieve a sustained and sequential release of desired drugs, and (3) the delivery vehicles can be assembled on any required implants and used any time postpreparation. These three requirements are satisfied by a facile and scalable strategy of the LbL self-assembly technique, which allows pH-triggered and impregnated microcapsules and PL/PG multilayer films to assemble into highly integrated and organized delivery vehicles to effectively load and sequentially release multiple drugs (e.g., AgNPs and rhBMP-2) to resolve two major complications of orthopedic bone injuries (i.e., infection and delayed bone regeneration).

Scheme 1 describes the synthesis pathway of our delivery vehicles of capsule-integrated PL/PG multilayer films. Biocompatible polypeptide PL and PG were selected as the building blocks to construct the delivery vehicles, and $CaCO_3$ particles were used as templates to assemble microcapsules. The as-prepared capsules were impregnated with PL or PG to create pH-triggered loading and release capability for positively and negatively charged drugs based on electrostatic interactions. To bring about further chemical bonding among PL and PG molecules in capsules, the shelled $CaCO_3$ particles were incubated using GA solution to form cross-linked shells, endowing the resultant microcapsules with sufficient stability without disassembly during template removal and drug loading. Moreover, abundant aldehyde groups were also introduced due to the excessive GA during this cross-linking process, which allowed effective integrating interaction between microcapsules and multilayer films.[22] Besides the microcapsules, by carefully controlling PL/PG multilayer films between different capsule layers, the sustained and precisely controlled release of different drugs with designed sequence, dose, and duration, could be achieved for drug delivery. Our capsule-integrated multilayer films were responsive to environmental pH. Such behavior allows for the development of smart therapies for injured tissues, which usually show varied pH values during the healing process, indicating a promising benefit in clinical practice for broad medical applications.[40–4] Using our previously reported open fracture rat model,[26] we measured the pH of tissue samples around infected and noninfected femurs l0 days after surgery, and their pH values were found to be approximately 7.0 and 6.5, respectively (Figure Sl). The pH was relatively low at the infection site, which was consistent with reports from other studies.[43–45] Bacteria like *Staphylococcus epidermidis* or *S. aureus* may create an acidic environment due to their metabolic production of acidic substances like lactic acid,[44] and local acidosis may occur due to massive infiltration of neutrophils and macrophages recruited to the site of infection.[45]

We selected microsized and porous $CaCO_3$ particles with diameter of ~6 μm to impregnate with PL or PG polypeptides, which can function as active loading sites and to further

assemble polypeptide shells for microcapsules. Figure 1a shows the typical $CaCO_3$ particles, on which abundant mesoporous pores were observed, meeting the requirements of rough surface, large surface area, and high porosity for polyelectrolyte impregnation. Upon incubating in 2 mg mL^{-1} of PL solution, the pore channels facilitated the penetration of solution into $CaCO_3$ particles due to capillary effect and led to the sufficient impregnation of PL molecules, which adsorbed not only on particle surfaces but also in the interior, and thus without being completely neutralized during subsequent LbL assembly.[46] Therefore, these excessive impregnated polyelectrolytes endowed the capsules with robust capacity to load charged drugs. As expected, the pore size and surface roughness decreased obviously after impregnation, further confirming the effective adhesion of PL polypeptides in $CaCO_3$ particles, as shown in Figure 1b. Further using the LbL self-assembly technique, PL and PG were alternatively deposited to form a shell of $(PL/PG)_{3.5}$ onto $CaCO_3$ particles, and the cross-linked nanofilm-shelled particles are illustrated in Figure 1c. SEM examinations were also conducted on dry shells after removal of $CaCO_3$ templates and confirmed the formation of microcapsules (Figure 1d). Figure 1e-g exhibits the typical formation process ranging from PL/PG multilayer film and shelled particle-integrated film to capsule-integrated film, revealing the successful hierarchical nano/microlevel self-assembly for our drug-delivery vehicles. In addition, evidence of structural change due to incorporation of capsules was also observed in AFM analyses (Figure 1h,i). The deposition of microcapsules led to an obvious increase in surface roughness, indicating a desirable topography to enhance the cell-material interactions for clinical applications.[11,47,48]

To elaborate on the growth profile of PL/PG multilayer films, we measured the absorbance of films on quartz slides using UV-vis spectrometry and the thickness of films on silicon wafers using ellipsometry, as shown in Figure 2a,b. With an increasing number of PL/PG bilayers, both the absorbance and thickness of multilayer films increased linearly, exhibiting a steady self-assembly process of charged polypeptides regardless of substrates. The average thickness of each bilayer was ~5.2 nm, which is consistent with our previous reports.[26,49] Moreover, the growth profiles and stability of PL/PG multilayer films fabricated from various solutions with different pH and sodium chloride (NaCl) contents were also studied, and the results showed that higher pH and NaCl concentration in solutions facilitated the assembly of polypeptide films; all assemblies exhibited good stability in PBS (Figure S2). In light of the crucial role of surface wettability on competitive protein adsorption and initial attachment of cells, we also investigated the correlation between hydrophilicity and the outermost structure of PL/PG multilayer films. Figure 2c presents the change in WCAs of films with different outermost layers. PL/ PG multilayer films with the outermost layer of PL exhibited WCAs of 45–49°, whereas WCAs of the PG outermost layer were much smaller and were within the range of 27–31° due to abundant side chain carboxyl groups of PG. The WCAs of PL/PG multilayer films increased slightly with increasing bilayer numbers, which could be attributed to the enhanced surface roughness according to the Cassie model.[50] A similar phenomenon was observed for the capsule-integrated $(PL/PG)_3$ multilayer films compared with $(PL/PG)_3$ films, further confirming the dominant contribution of microcapsules on the construction of hierarchical roughness of delivery coatings.

To evaluate the mechanical properties of our designed delivery vehicles, we prepared capsule-integrated multilayer films on K-wires and tested their stability using our in vivo rat model.[51] The SEM result of the most severely damaged parts of the coating film on a K-wire is illustrated in Figure 2d. After analyzing the thickness, regularity, and damage to the whole films before and after implantation, we found that most damage occurred on the front part of the coating on K-wires, which suffered the most abrasion during the drilling process into the rat femur; more than 85% of the films withstood the implantation process in our in vivo rat model. In addition, the long-term stability of the capsule-integrated polypeptide films in solution was evaluated. As shown in Figures S3 and S4, no obvious changes were observed in both film thickness and capsule structure after immersing the films in PBS for up to 10 days.

We aimed to employ the microcapsules as the primary vehicles for drug delivery. Consequently, our delivery vehicles were mainly designed in terms of the preimpregnation capacity of polypeptides in $CaCO_3$ particles and particle density in the delivery systems. We determined drug loading and release in the multilayer films using the fluorescence labeling method. Although the particle density on multilayer films was almost the same (Figure 3a'-c'), the fluorescence intensity of particle-integrated films significantly improved with increasing incubation time (from 5 to 30 min) of $CaCO_3$ particles in 2 mg mL^{-1} of PL-FITC solution, as presented in Figure 3a-c. Plotting the amount of PL-FITC in $CaCO_3$ particles versus their incubation time revealed that the impregnation achieved saturation with incubation time of 20 min, and ~3.8 ng per particle of PL was impregnated, as shown in Figure 3d. This result was further confirmed by the SEM analysis of $CaCO_3$ particles with fully blocked pores (Figure 1b). Figure 3e-g,e'- g' shows the assembly of shelled $CaCO_3$ particles on $(PL/PG)_5$ multilayer films incubated in $CaCO_3^{PL\text{-}FITC}$ particle suspension with various times. With increasing incubation time from 10 to 180 min (Figure 3h), the particles on films exhibited distribution densities of 800, 2490, 8160, 12 300, 14 500, and 15 100 cm^{-2}, revealing that the incubation time of 120 min was enough to endow saturated particle assembly in our delivery vehicles. To provide insight into the successful assembly of preimpregnated capsules, we also performed in situ CLSM observation for our delivery vehicles before and after $CaCO_3$ template removal (Figure 3i-k); the results indicated that most impregnated PL polypeptides remained after $CaCO_3$ decomposition. Figure 3l illustrates the morphology of our developed delivery vehicles of $(PL/PG)_5$/ $capsule^{PL\text{-}FITC}$/PG/$(PL/PG)_8$, suggesting a uniform distribution of capsules in the PL/PG multilayer films.

3.2. Multiple Drug-Loading and Release Studies.

After optimizing the hierarchical structures of multilayer films, we assessed the delivery capability for multiple drugs of very different properties. Fluorescently labeled BSA and histone were studied as two model drugs. BSA with isoelectric point (pi) of ~5, a negatively charged drug model under pH = 7.4, could be easily loaded into $L_5/C^G/L_8/C^L/L_8$ delivery vehicles, which is visualized under CLSM, as shown in Figure 4a-c. To confirm the detailed loading location, both capsules and BSA were fluorescence labeled, and the results are shown in Figure S5. The green fluorescent spots (i.e., PL-FITC; Figure S5a-c) overlapped with the red fluorescent ones (i.e., Alexa Fluor 647- conjugated BSA; Figure S5a'-c'),

indicating the successful loading of BSA within PL-impregnated capsules in our delivery vehicles. The $L_5/C^G/L_8/C^L/L_8$ films also functioned as delivery vehicles for loading the positively charged drug model of Alexa Fluor 488-conjugated histone H1 from calf thymus (pi ~ 11.3), as illustrated in Figure 4d-f. Moreover, BSA and histone loading were both facilely tunable, for instance, via a simple control of incubation time (Figure 4g,h). With increasing incubation time from 2 to 20 min, the fluorescence intensity of our drug-loaded delivery vehicles increased significantly (Figure 4a-c,d-f). Loading of BSA reached a maximum of ~80 μg cm^{-2} at 20 min incubation, whereas histone loading showed a higher value of 100 μg cm^{-2} at 20 min incubation, as exhibited in Figure 4g,h. Besides the loading capability after vehicle preparation, it is worth noting that both of these two loading processes of our delivery vehicles were mostly finished within 10 min, revealing their fast loading capacity and robust clinical application potential, such as realization of controlled drug loading just minutes before surgical implantation, which has been rarely reported previously.[22]

We further examined the release profiles of multiple drugs to reveal the tunability and kinetics of drug release from PL/PG delivery vehicles with different hierarchical structures. Here, pH was employed as a means of controlling the loading and release of multiple drugs: loading under a large pH gap above/ below pi of drugs by virtue of the electrostatic attraction driven from resultant net charges and release under pH similar to pI of drugs due to disappearance of “binding sites” based on reduced net charges, which was confirmed by our previous studies.[37,49] As demonstrated in Figure 5a,b, an obvious release within 1 day of BSA and histone was triggered due to pH variation, followed by sustained release behavior, for delivery vehicles integrated with capsule^{PL} and capsule^{PG}, respectively. However, very little loading and release of BSA (7 μg cm^{-2}) and of histone (8 μg cm^{-2}) were found in PL/PG multilayer films without capsules and like-charged capsules. The comparison of release profiles between vehicles with and without capsule^{PL}/capsule^{PG} suggested that the delivery process was governed mainly by electrostatic interactions derived from the impregnated capsules with opposite charges. With an increasing number of PL/PG bilayers as the outermost layers of the films ranging from 3 to 8 to 13, the “burst effect” of drug release was significantly weakened, which could be attributed to the shielding effect from shell-like PL/PG multilayer films. For instance, the release of BSA within the 1st day from $L_5/C^G/L_8/C^L/L_3$ films was 50 μg cm^{-2}, whereas that from $L_5/C^G/L_8/C^L/L_{13}$ films was 32 μg cm^{-2}, showing a 35% decrease of “burst release” compared with the former one. This result suggests an effective strategy to tune the drug release profiles for achieving a progressive release from capsule- based delivery vehicles. $L_5/C^G/L_8/C^L/L_{13}$ delivery vehicles showed a total release of ~71 μg cm^{-2} within 14 days (Figure 5a). Similarly, ~48 μg cm^{-2} of histone was released from $L_5/C^G/L_{13}/C^L/L_8$ films within 7 days, and ~85 μg cm^{-2} was released within almost 6 weeks. Moreover, compared with $L_5/C^G/L_8/C^L/L_8$ films drug-loaded for 15 min, the capsule-integrated films incubated with less time (5 min) exhibited a similar release tendency but with a proportional reduction, further confirming the controllable drug-loading capacity of our delivery vehicles by adjusting the drug incubation time. In addition, the releases of BSA and histone from $L_5/C^G/L_8/C^L/L_8$ films immersed in SBF were found to be 43 and 36 μg cm^{-2}, respectively, within the 1st day, and reached ~68 μg cm^{-2} of BSA and ~67 μg cm^{-2} of histone within 10 days (Figure S6).

3.3. Anti-infection Capacity Evaluation.

Recently, a promising antimicrobial agent, AgNPs, is emerging as a new treatment option against a wide array of pathogens.[52–54] In this work, we used PVP-capped AgNPs as a delivery drug to endow our vehicles with the capability of preventing postoperative infection which may be less likely to induce resistance, a challenge in dental and orthopedic surgeries.[55,56] First, the physicochemical properties of our AgNPs were analyzed for their size distribution and ζ potential. Over 80% of AgNPs were in the range of 8–25 nm with an average value of 13.5 nm (Figure 6a), and a normalized three-dimensional (3D) graph (size vs intensity vs concentration) was also presented (inset of Figure 6a). As illustrated in Figure 6b, the surface ζ potential of AgNPs was determined to be −14.9 ± 0.3 mV, indicating their loading capacity to capsule^{PL}-based delivery vehicles through electrostatic interactions. By measuring the absorption spectra at 410 nm, the release profile of AgNP from our delivery vehicles was also evaluated. As shown in Figure S7a, the delivery vehicle of $L_5/C^G/L_8/C^L/L_8$ film, which was loaded in 0.1 mg mL^{-1} of AgNP suspension for 40 min, showed a release of ~18 μg cm^{-2} AgNP within the 1st day and reached a total release of ~40 μg cm^{-2} after 2 weeks. To quantitatively characterize the antibacterial activity of our delivery vehicles encapsulated with AgNPs, we carried out in vitro bacterial assays toward *S. aureus* using various delivery vehicles with different hierarchical structures. The obtained *S. aureus* killing efficacy is shown in Figure 6c. The antibacterial activities of L_{23} and $L_5/C^G/L_8/C^L/L_8$ films were negligible with a calculated efficacy of ~2%. This result could be attributed to the disordered topography arising from surface roughness of the polypeptide PL layers, which was consistent with other studies.[9,57] Compared to these two control delivery vehicles, the $L_5/C^G/L_8/C^{L+AgNPs}/L_8$ films loaded in 0.1 mg mL^{-1} of AgNP suspension showed an obvious antibacterial activity with dose-dependent killing efficacy. The AgNP-loaded vehicles with different incubation time ranging from 5, 20, 40, and 60 min exhibited killing efficiencies of 26.8, 49.3, 72.5, and 83.1%, respectively, suggesting an effective strategy for preventing implant infection by loading of AgNPs in our designed capsule-integrated multilayer films. Also, the successful loading of AgNPs further confirmed the robust delivery capability of our developed vehicles to deliver multiple drugs with very different properties, even particles, in a post-preparation loading manner. To compare the efficacy of AgNPs released from $L_5/C^G/L_8/C^{L+AgNPs}/L_8$ film and in original suspension, we studied the killing efficacy of AgNP original suspension: these AgNPs exhibited strong antibacterial activity against *S. aureus*, displaying killing efficacies of 42.5% at 20 μM and 99.4% at 93 μM in solutions.

Generally, concern about the toxicity of AgNPs has limited their clinical use.[58,59] In this study, human osteoblast viability using the Trypan blue assay was conducted to determine the toxicity of various delivery vehicles encapsulated with/without AgNPs and control AgNP suspensions, as shown in Figure 6d. Excellent viability of osteoblasts (~95%) was observed using L_{23} and $L_5/C^G/L_8/C^L/L_8$ films without AgNP loading due to their good biocompatibility from polypeptides. Compared to the 93 μM AgNP suspension, the decreased concentration (20 μM) led to significantly low toxicity to osteoblast cells with a viability of 92%. Our delivery vehicles of $L_5/C^G/L_8/C^{L+AgNPs}/L_8$ films loaded with AgNPs with different incubation time of 5, 20, 40, and 60 min achieved viabilities of 90, 92, 90, and 85%, respectively, suggesting their low toxicity toward human cells yet with similar *S.*

aureus killing efficacy as AgNP suspensions. The phenomenon could be attributed to the strategy of using delivery vehicles with sustained release capacity rather than a one-time and high-concentration release which may greatly decrease the toxicity to osteoblasts while keep an effective dose for killing bacteria, which was consistent with other studies.[26,60]

3.4. Bone Regeneration Capacity Evaluation.

Up to now, although rhBMP-2 presents outstanding regenerative properties for bone regeneration, the clinical utilization of its delivery system has been associated with severe side effects due to noncontrolled delivery and nonbiocompatible vehicles.[61,62] Here, our PL/PG-based capsule-integrated multilayer films provided an effective, biocompatible, and fully resorbable delivery vehicle for a pH-responsive release of rhBMP-2. On the basis of ELISA tests (Figure S7b), the drug-loaded $L_5/C^G/L_8/C^L/L_8$ films, which were incubated in 4 μg mL^{-1} of rhBMP- 2 solutions for 20 min, achieved a release of ~20.5 μg cm^{-2} rhBMP-2 within the 1st day and obtained a total release of ~55 μg cm^{-2} within 6 weeks, further demonstrated a robust delivery capacity of our delivery vehicles to achieve a sustained release. As illustrated in Figure 7a, compared to the uncoated quartz slides, substantially more osteoblast cells were attached on the slides coated with polypeptide nanofilms. The PL/PG multilayer films with and without capsules had a similar change of cell density within the 12 h culture time; meanwhile, capsule-integrated films loaded with rhBMP-2 showed a significant increase in cell density at 4, 8, and 12 h compared to the two control systems, and their cell density increased with increasing incubation time in rhBMP-2 solution. For example, at 4 h, the cell densities on quartz slides, L_{23} films, $L_5/C^G/L_8/C^l/L_8$ films, and $L_5/C^{G+bmp}/L_8/C^l/L_8$ films incubated in rhBMP-2 solution for 5 and 15 min, were 500, 3500, 4000, 6800, and 8200 cell cm^{-2}, respectively. At 12 h, the cell density on capsule-integrated films loaded with rhBMP-2 for 15 min achieved 13500 cell cm^{-2}, indicating a rapid and enhanced cell adhesion by virtue of the combination effect from hierarchical surface structure and rhBMP-2 stimulation. Figure 7b shows the proliferation of osteoblast cells on different culture surfaces at 1, 3, and 5 days. The cell proliferation was significantly enhanced on polypeptide films compared to control quartz slides. For instance, after 3 days, the cell densities on quartz slides, L_{23} films, $L_5/C^G/L_8/C^l/L_8$ films, $L_5/C^{G+bmp}/L_8/C^l/L_8$ films loaded with rhBMP-2 for 5 and 15 min, were 6000, 16 200, 17 500, 24 200, and 26 500 cell cm^{-2}, respectively. For L_{23} and $L_5/C^G/L_8/C^l/L_8$ films, cell proliferation slowed down from 3 to 5 days compared to that from 1 to 3 days. For rhBMP-2-loaded capsule-integrated vehicles, a rapid and sustained cell growth was observed from 1 to 5 days, and high cell densities of 28 000 and 34 200 cell cm^{-2} were obtained at 5 days, respectively, further confirming the bone regeneration effect from controlled and sustained release of rhBMP-2 in our capsule-integrated delivery vehicles. Moreover, the percentages of live osteoblast cells on polypeptide films without rhBMP-2 and control quartz slides were about the same and were in the range of 70–75% at 1, 3, and 5 days; whereas those of rhBMP-2-encapsulated PL/PG delivery vehicles were significantly higher and were in the range of 90–95% (Figure 7c). This result indicated that, compared to the control quartz sides and PL/PG films, the encapsulation of rhBMP-2 had shown higher osteoblast cell viability. In addition, Figure 7d presents osteoblast cell adhesion on various culture surfaces mentioned in Figure 7b,c at 1 day. Obviously, a growing number of cells attached on the culture surfaces ranging from quartz slides and PL/PG films to capsule-integrated films without and with rhBMP-2

(Figure 7d-i-v), and better cell spread was achieved on polypeptide films (especially on rhBMP-2 loaded delivery films) compared to the uncoated quartz slides. The detailed SEM image showing the firm adhesion of osteoblast cells on polypeptide films is illustrated in Figure 7d-vi.

4. CONCLUSIONS

In summary, we have, for the first time, presented a robust strategy for creating innovative vehicles assembled by polypeptide capsules and multilayer films to deliver multiple drugs via the LbL self-assembly technique, for preventing implant-associated infections and promoting bone regeneration. High, precisely controlled, and postpreparation loading capacity was achieved via creating polyelectrolyte-impregnated microcapsules functioning as the main delivery vehicles, whereas on-demand and sustained release in patient-specific time sequences was further designed by integrating microcapsules into multilayer films. Four very different drugs including BSA, histone, AgNPs, and rhBMP-2 were successfully loaded into the capsule-integrated multilayer films at any time post-preparation and exhibited high and controllable loading (for instance, 80 μg cm^{-2} of BSA and 100 μg cm^{-2} of histone) and sustained release profiles (up to 2 weeks or longer). With the robust and controlled loading and release capacity for multiple drugs driven by the hierarchical nano/microlevel structures, our designed delivery vehicles achieved a *S. aureus* killing efficacy of 83% while maintaining an osteoblast viability of >85% using AgNP delivery. Our delivery vehicles had more than 10-fold cell adhesion capability within 4 h, 5fold cell proliferation capability within 5 days, and greatly enhanced live cell percentage of >90% with successful delivery of rhBMP-2. We believe that such delivery vehicles based on capsule-integrated multilayer films will open up numerous opportunities for a range of orthopedic surgery applications, such as musculoskeletal trauma, spine diseases, sports injuries, degenerative diseases, infections, congenital disorders, and so on.

Supplementary Material

Refer to Web version on PubMed Central for supplementary material.

ACKNOWLEDGMENTS

This work is supported by the Office of the Assistant Secretary of Defense for Health Affairs, through the Peer Reviewed Medical Research Program, Discovery Awards under Award Nos. W81XWH-17–1-0603 and W81XWH1810203. We also acknowledge financial support from AO Foundation, Osteosynthesis & Trauma Care Foundation, the West Virginia National Aeronautics and Space Administration Experimental Program to Stimulate Competitive Research (WV NASA EPSCoR), WVU PSCOR, and WVCTSI. In addition, we acknowledge the use of the WVU Shared Research Facilities that are supported by NIH grants 2U54GM104942–02, 5P20RR016477, U57GM104942, P30GM103488, P20GM109098, and P20GM103434. Opinions, interpretations, conclusions, and recommendations are those of the authors and are not necessarily endorsed by the funding agencies. We also acknowledge Suzanne Danley for proofreading.

REFERENCES

(1). Doloff JC; Veiseh O; Vegas AJ; Tam HH; Farah S; Ma M; Li J; Bader A; Chiu A; Sadraei A; et al. Colony Stimulating Factor-1 Receptor is a Central Component of the Foreign Body Response to Biomaterial Implants in Rodents and Non-Human Primates. Nat. Mater. 2017, 16, 671–680. [PubMed: 28319612]

(2). Cobelli N; Scharf B; Crisi GM; Hardin J; Santambrogio L Mediators of the Inflammatory Response to Joint Replacement Devices. Nat. Rev. Rheumatol. 2011, 7, 600–608. [PubMed: 21894210]

(3). Hubbell JA; Langer R Translating Materials Design to the Clinic. Nat. Mater. 2013, 12, 963–966. [PubMed: 24150414]

(4). Nichols SP; Koh A; Storm WL; Shin JH; Schoenfisch MH Biocompatible Materials for Continuous Glucose Monitoring Devices. Chem. Rev. 2013, 113, 2528–2549. [PubMed: 23387395]

(5). Yang Y; Ao H; Wang Y; Lin W; Yang S; Zhang S; Yu Z; Tang T Cytocompatibility with Osteogenic Cells and Enhanced in vivo Anti-Infection Potential of Quaternized Chitosan-Loaded Titania Nanotubes. Bone Res. 2016, 4, No. 16027.

(6). Zimmerli W Clinical Presentation and Treatment of Orthopaedic Implant-Associated Infection. J. Intern. Med. 2014, 276, 111–119. [PubMed: 24605880]

(7). Arciola CR; Campoccia D; Montanaro L Implant Infections: Adhesion, Biofilm Formation and Immune Evasion. Nat. Rev. Microbiol. 2018, 16, 397–409. [PubMed: 29720707]

(8). Min J; Choi KY; Dreaden EC; Padera RF; Braatz RD; Spector M; Hammond PT Designer Dual Therapy Nanolayered Implant Coatings Eradicate Biofilms and Accelerate Bone Tissue Repair. ACS Nano 2016, 10, 4441–4450. [PubMed: 26923427]

(9). Jiang B; Li B Polypeptide Nanocoatings for Preventing Dental and Orthopaedic Device-Associated Infection: pH-Induced Antibiotic Capture, Release, and Antibiotic Efficacy. J. Biomed. Mater. Res. Part B 2009, 88B, 332–338.

(10). Jiang B; Barnett JB; Li B Advances in Polyelectrolyte Multilayer Nanofilms as Tunable Drug Delivery Systems. Nano- technolj Sci. Appl 2009, 2, 21–27.

(11). Likibi F; Jiang B; Li B Biomimetic Nanocoating Promotes Osteoblast Cell Adhesion on Biomedical Implants. J. Mater. Res. 2008, 23, 3222–3228.

(12). Raphel J; Holodniy M; Goodman SB; Heilshorn SC Multifunctional Coatings to Simultaneously Promote Osseointegra- tion and Prevent Infection of Orthopaedic Implants. Biomaterials 2016, 84, 301–314. [PubMed: 26851394]

(13). Tatara AM; Kontoyiannis DP; Mikos AG Drug Delivery and Tissue Engineering to Promote Wound Healing in the Immunocompromised Host: Current Challenges and Future Directions. Adv. Drug Delivery Rev. 2018, 129, 319–329.

(14). Richardson JJ; Bjornmalm M; Caruso F Multilayer Assembly. Technology-Driven Layer-by-Layer Assembly of Nanofilms. Science 2015, 348, No. aaa2491.

(15). Borges J; Sousa MP; Cinar G; Caridade SG; Guler MO; Mano JF Nanoengineering Hybrid Supramolecular Multilayered Biomaterials using Polysaccharides and Self-Assembling Peptide Amphiphiles. Adv. Funct. Mater. 2017, 27, No. 1605122.

(16). Keeney M; Jiang XY; Yamane M; Lee M; Goodman S; Yang F Nanocoating for Biomolecule Delivery using Layer-by-Layer Self-Assembly. J. Mater. Chem. B 2015, 3, 8757–8770. [PubMed: 27099754]

(17). Zhang S; Xing M; Li B Biomimetic Layer-by-Layer Self-Assembly of Nanofilms, Nanocoatings, and 3D Scaffolds for Tissue Engineering. Int. J. Mol. Sci. 2018, 19, 1641.

(18). Shi D; Ran M; Zhang L; Huang H; Li X; Chen M; Akashi M Fabrication of Biobased Polyelectrolyte Capsules and Their Application for Glucose-Triggered Insulin Delivery. ACS Appl. Mater. Interfaces 2016, 8, 13688–13697. [PubMed: 27210795]

(19). Tang Y; Heaysman CL; Willis S; Lewis AL Physical Hydrogels with Self-Assembled Nanostructures as Drug Delivery Systems. Expert Opin. Drug Delivery 2011, 8, 1141–1159.

(20). Han L; Tang C; Yin C Dual-Targeting and pH/Redox- Responsive Multi-Layered Nanocomplexes for Smart Co-Delivery of Doxorubicin and siRNA. Biomaterials 2015, 60, 42–52. [PubMed: 25982552]

(21). Arai N; Yasuoka K; Zeng XC Self-Assembly of Janus Oligomers into Onion-like Vesicles with Layer-by-Layer Water Discharging Capability: A Minimalist Model. ACS Nano 2016, 10, 8026–8037. [PubMed: 27466700]

(22). Jiang B; Defusco E; Li B Polypeptide Multilayer Film Co Delivers Oppositely-Charged Drug Molecules in Sustained Manners. Biomacromolecules 2010, 11, 3630–3637. [PubMed: 21058719]

(23). Kim BS; Park SW; Hammond PT Hydrogen-Bonding Layer-by-Layer-Assembled Biodegradable Polymeric Micelles as Drug Delivery Vehicles from Surfaces. ACS Nano 2008, 2, 386–392. [PubMed: 19206641]

(24). De Cock LJ; De Koker S; De Geest BG; Grooten J; Vervaet C; Remon JP; Sukhorukov GB; Antipina MN Polymeric Multilayer Capsules in Drug Delivery. Angew. Chem., Int. Ed. 2010, 49, 6954–6973.

(25). Lin X; Wu Z; Wu Y; Xuan M; He Q Self-Propelled Micro-/Nanomotors Based on Controlled Assembled Architectures. Adv. Mater. 2016, 28, 1060–1072. [PubMed: 26421653]

(26). Li B; Jiang B; Boyce BM; Lindsey BA Multilayer Polypeptide Nanoscale Coatings Incorporating IL-12 for the Prevention of Biomedical Device-Associated Infections. Biomaterials 2009, 30, 2552–2558. [PubMed: 19215980]

(27). Berg MC; Zhai L; Cohen RE; Rubner MF Controlled Drug Release from Porous Polyelectrolyte Multilayers. Biomacromolecules 2006, 7, 357–364. [PubMed: 16398536]

(28). Liu G; Li L; Huo D; Li Y; Wu Y; Zeng L; Cheng P; Xing M; Zeng W; Zhu C A VEGF Delivery System Targeting MI Improves Angiogenesis and Cardiac Function Based on the Tropism of MSCs and Layer-by-Layer Self-Assembly. Biomaterials 2017, 127, 117–131. [PubMed: 28284103]

(29). Li Z; Yuan D; Jin G; Tan BH; He C Facile Layer-by- Layer Self-Assembly toward Enantiomeric Poly(lactide) Stereo-complex Coated Magnetite Nanocarrier for Highly Tunable Drug Deliveries. ACS Appl. Mater. Interfaces 2016, 8, 1842–1853. [PubMed: 26717323]

(30). Lei W.-x.; Chen X.-c.; Hu M; Chang H; Xu H; Ren K.-f.; Ji J Dynamic Spongy Films to Immobilize Hydrophobic Antimicrobial Peptides for Self-Healing Bactericidal Coating. J. Mater. Chem. B 2016, 4, 6358–6365.

(31). Delcea M; Mohwald H; Skirtach AG Stimuli-Responsive LbL Capsules and Nanoshells for Drug Delivery. Adv. Drug Delivery Rev. 2011, 63, 730–747.

(32). Hong J; Char K; Kim B-S Hollow Capsules of Reduced Graphene Oxide Nanosheets Assembled on a Sacrificial Colloidal Particle. J. Phys. Chem. Lett. 2010, 1, 3442–3445.

(33). Wood KC; Chuang HF; Batten RD; Lynn DM; Hammond PT Controlling Interlayer Diffusion to Achieve Sustained, Multiagent Delivery from Layer-by-Layer Thin Films. Proc. Natl. Acad. Sci 2006, 103, 10207–10212. [PubMed: 16801543]

(34). Soike T; Streff AK; Guan C; Ortega R; Tantawy M; Pino C; Shastri VP Engineering a Material Surface for Drug Delivery and Imaging using Layer-by-Layer Assembly of Function-alized Nanoparticles. Adv. Mater. 2010, 22, 1392–1397. [PubMed: 20437489]

(35). Ramasamy T; Haidar ZS; Tran TH; Choi JY; Jeong JH; Shin BS; Choi H-G; Yong CS; Kim JO Layer-by-Layer Assembly of Liposomal Nanoparticles with Pegylated Polyelectrolytes Enhances Systemic Delivery of Multiple Anticancer Drugs. Acta Biomater. 2014, 10, 5116–5127. [PubMed: 25169256]

(36). Gong M-Q; Wu J-L; Chen B; Zhuo R-X; Cheng S-X Self-Assembled Polymer/Inorganic Hybrid Nanovesicles for Multiple Drug Delivery to Overcome Drug Resistance in Cancer Chemotherapy. Langmuir 2015, 31, 5115–5122. [PubMed: 25927163]

(37). Zhao Q; Li B pH-Controlled Drug Loading and Release from Biodegradable Microcapsules. Nanomedicine 2008, 4, 302–310. [PubMed: 18657478]

(38). Blanco E; Shen H; Ferrari M Principles of Nanoparticle Design for Overcoming Biological Barriers to Drug Delivery. Nat. Biotechnol. 2015, 33, 941–951. [PubMed: 26348965]

(39). Habibi N; Kamaly N; Memic A; Shafiee H Self-Assembled Peptide-Based Nanostructures: Smart Nanomaterials toward Targeted Drug Delivery. Nano Today 2016, 11, 41–60. [PubMed: 27103939]

(40). Guinovart T; Valdes-Ramirez G; Windmiller JR; Andrade FJ; Wang J Bandage-Based Wearable Potentiometric Sensor for Monitoring Wound pH. Electroanalysis 2014, 26, 1345–1353.

(41). Ono S; Imai R; Ida Y; Shibata D; Komiya T; Matsumura H Increased Wound pH as an Indicator of Local Wound Infection in Second Degree Burns. Burns 2015, 41, 820–824. [PubMed: 25468471]

(42). Anandhakumar S; Gokul P; Raichur A Stimuli-Responsive Weak Polyelectrolyte Multilayer Films: A Thin Film Platform for Self Triggered Multi-Drug Delivery. Mater. Sci. Eng. C 2016, 58, 622–628.

(43). Pichavant L; Amador G; Jacqueline C; Brouillaud B; Heroguez V; Durrieu M-C pH-Controlled Delivery of Gentamicin Sulfate from Orthopedic Devices Preventing Nosocomial Infections. J. Controlled Release 2012, 162, 373–381.

(44). Pavlukhina S; Lu Y; Patimetha A; Libera M; Sukhishvili S Polymer Multilayers with pH-Triggered Release of Antibacterial Agents. Biomacromolecules 2010, 11, 3448–3456. [PubMed: 21028796]

(45). Md BB Systemic Response to Inflammation. Nutr. Rev. 2007, 65, S170–S172. [PubMed: 18240543]

(46). Cai J; Perfect E; Cheng C-L; Hu X Generalized Modeling of Spontaneous Imbibition Based on Hagen-Poiseuille Flow in Tortuous Capillaries with Variably Shaped Apertures. Langmuir 2014, 30, 5142–5151. [PubMed: 24785579]

(47). Yang L; Gong Z; Lin Y; Chinthapenta V; Li Q; Webster TJ; Sheldon BW Disordered Topography Mediates Filopodial Extension and Morphology of Cells on Stiff Materials. Adv. Funct. Mater. 2017, 27, No. 1702689.

(48). Viswanathan P; Ondeck MG; Chirasatitsin S; Ngamkham K; Reilly GC; Engler AJ; Battaglia G 3D Surface Topology Guides Stem Cell Adhesion and Differentiation. Biomaterials 2015, 52, 140–147. [PubMed: 25818420]

(49). Jiang B; Li B Tunable Drug Loading and Release from Polypeptide Multilayer Nanofilms. Int. J. Nanomed. 2009, 4, 37–53.

(50). Yang C; Tartaglino U; Persson B Influence of Surface Roughness on Superhydrophobicity. Phys. Rev. Lett. 2006, 97, No. 116103.

(51). Hamza T; Dietz M; Pham D; Clovis N; Danley S; Li B Intra-Cellular Staphylococcus aureus Alone Causes Infection in Vivo. Eur. Cell Mater. 2013, 25, 341–350. [PubMed: 23832687]

(52). Franci G; Falanga A; Galdiero S; Palomba L; Rai M; Morelli G; Galdiero M Silver Nanoparticles as Potential Antibacterial Agents. Molecules 2015, 20, 8856–8874. [PubMed: 25993417]

(53). Le Ouay B; Stellacci F Antibacterial Activity of Silver Nanoparticles: A Surface Science Insight. Nano Today 2015, 10, 339–354.

(54). Durán N; Durán M; de Jesus MB; Seabra AB; Fávaro WJ; Nakazato G Silver Nanoparticles: A New View on Mechanistic Aspects on Antimicrobial Activity. Nanomedicine 2016, 12, 789–799. [PubMed: 26724539]

(55). Li B; Webster TJ Bacteria Antibiotic Resistance: New Challenges and Opportunities for Implant-Associated Orthopedic Infections. J. Orthop. Res. 2018, 36, 22–32. [PubMed: 28722231]

(56). Li H; Li B PRP as a New Approach to Prevent Infection: Preparation and in vitro Antimicrobial Properties of PRP. J. Visualized Exp. 2013, 74, No. 50351.

(57). Guyomard A; De E; Jouenne T; Malandain JJ; Muller G; Glinel K Incorporation of a Hydrophobic Antibacterial Peptide into Amphiphilic Polyelectrolyte Multilayers: A Bioinspired Approach to Prepare Biocidal Thin Coatings. Adv. Funct. Mater. 2008, 18, 758–765.

(58). Stensberg MC; Wei Q; McLamore ES; Porterfield DM; Wei A; Sepulveda MS Toxicological Studies on Silver Nanoparticles: Challenges and Opportunities in Assessment, Monitoring and Imaging. Nanomedicine 2011, 6, 879–898. [PubMed: 21793678]

(59). AshaRani P; Mun GLK; Hande MP; Valiyaveettil S Cytotoxicity and Genotoxicity of Silver Nanoparticles in Human Cells. ACS Nano 2009, 3, 279–290. [PubMed: 19236062]

(60). Li H; Ogle H; Jiang B; Hagar M; Li B Cefazolin Embedded Biodegradable Polypeptide Nanofilms Promising for Infection Prevention: A Preliminary Study on Cell Responses. J. Orthop. Res. 2010, 28, 992–999. [PubMed: 20162715]

(61). Quinlan E; Thompson EM; Matsiko A; O'brien FJ; López-Noriega A Long-Term Controlled Delivery of Rhbmp-2 from Collagen-Hydroxyapatite Scaffolds for Superior Bone Tissue Regeneration. J. Controlled Release 2015, 207, 112–119.

(62). Tannoury CA; An HS Complications with the Use of Bone Morphogenetic Protein 2 (BMP-2) in Spine Surgery. Spine J. 2014, 14, 552–559. [PubMed: 24412416]

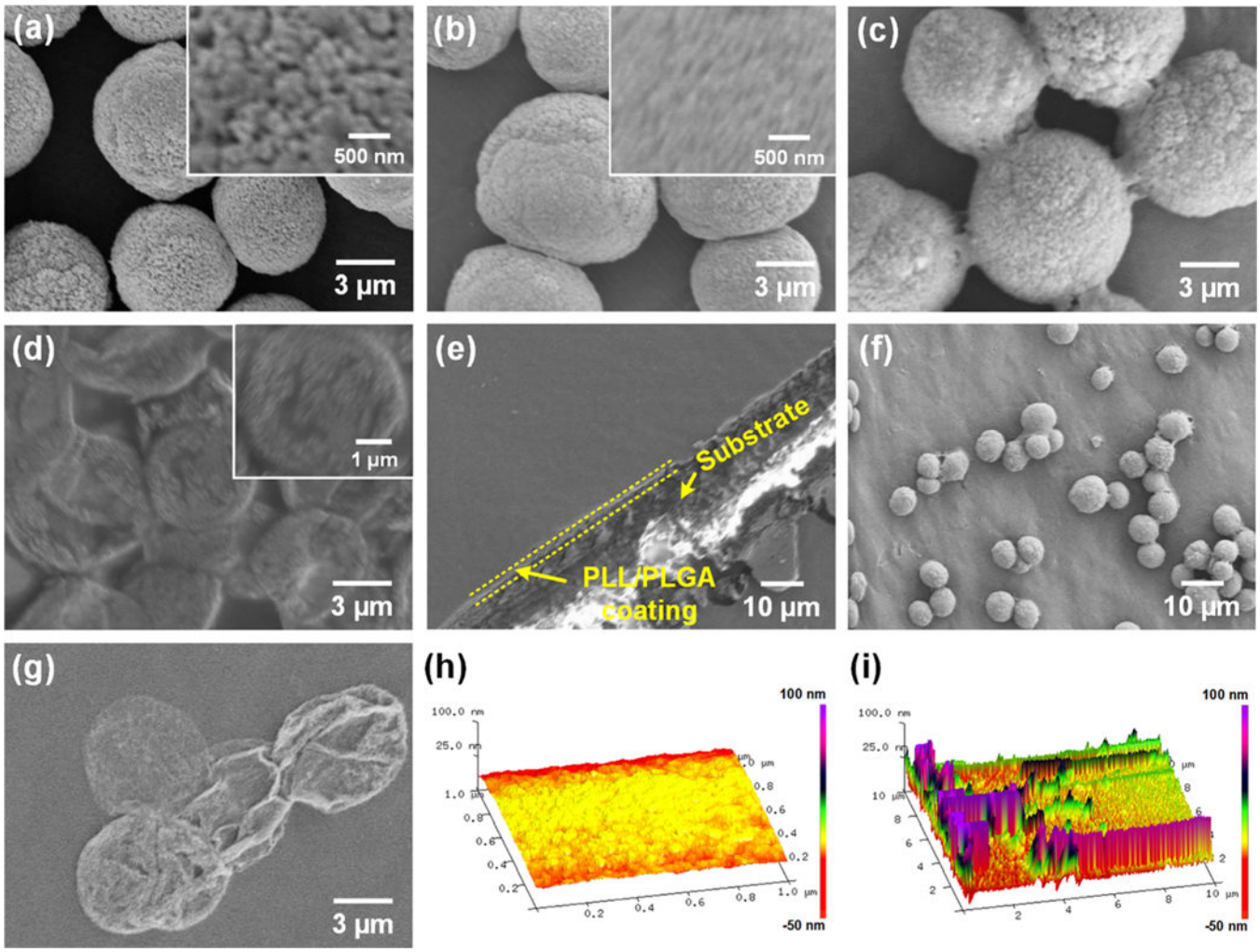

Figure 1.

SEM images of (a) $CaCO_3$ template particles, (b) $CaCO_3^{PL}$ particles, (c) cross-linked $(PL/PG)_{3.5}$ nanofilm-shelled $CaCO_3^{PL}$ particles, (d) capsule^{PL}, (e) $(PL/PG)_5$ multilayer nanofilm, (f) shelled $CaCO_3$ particles on $(PL/PG)_5$ film, and (g) capsule^{PL} on $(PL/PG)_5$ nanofilm. AFM images of the zone (h) without and (i) with capsules on capsule^{PL}-integrated $(PL/PG)_5$ multilayer films.

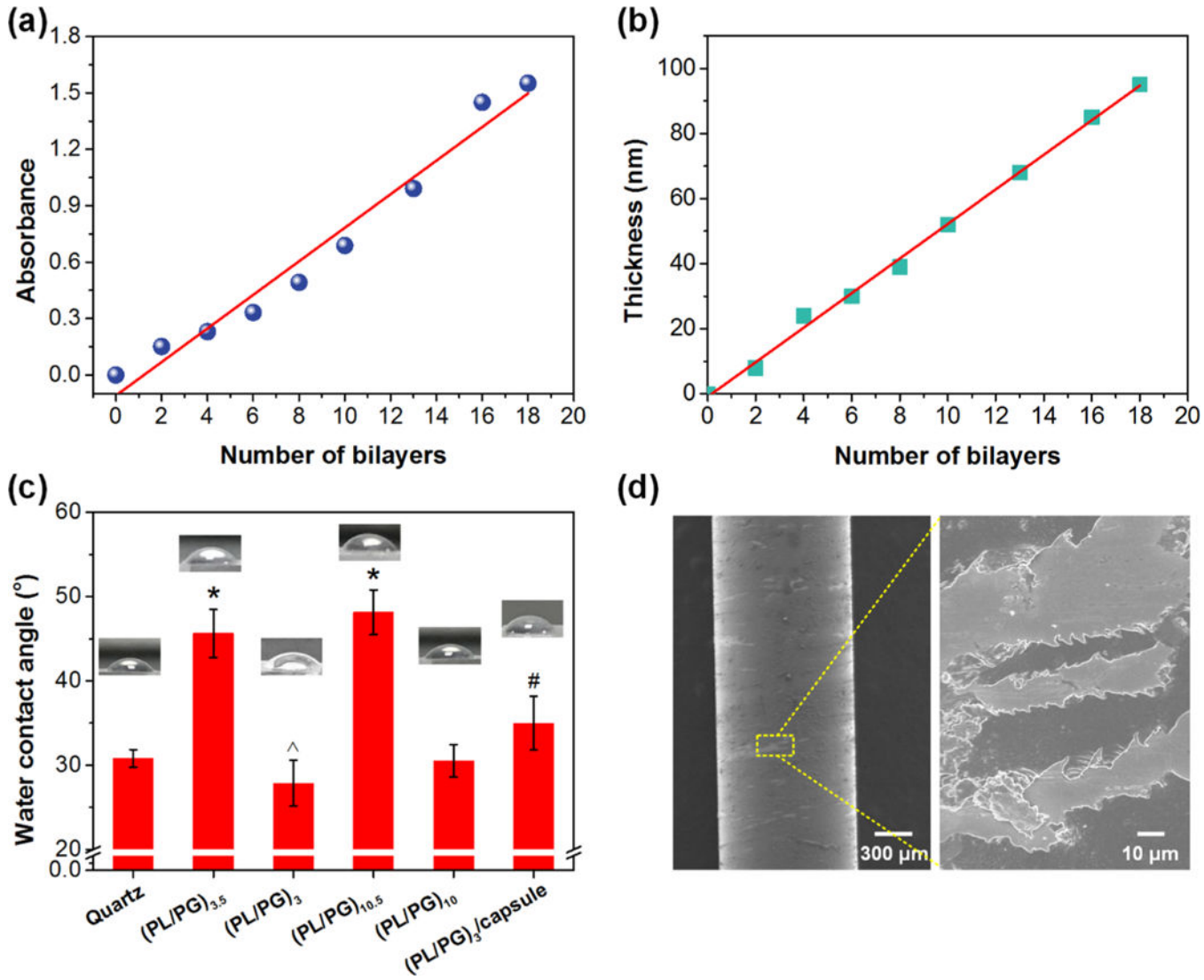

Figure 2.

Growth profiles of PL/PG multilayer nanofilms (a) on quartz slides using UV-vis spectrometry and (b) on silicon wafers using ellipsometry. (c) WCAs of quartz slides without and with different PL/PG multilayer nanofilms. (d) SEM images of nanoscale coatings on K-wire after implantation. * $p < 0.001$ compared to quartz, ^ $p < 0.001$ compared to $(PL/PG)_{3\ 5}$ film, # $p < 0.01$ compared to $(PL/PG)_3$ film.

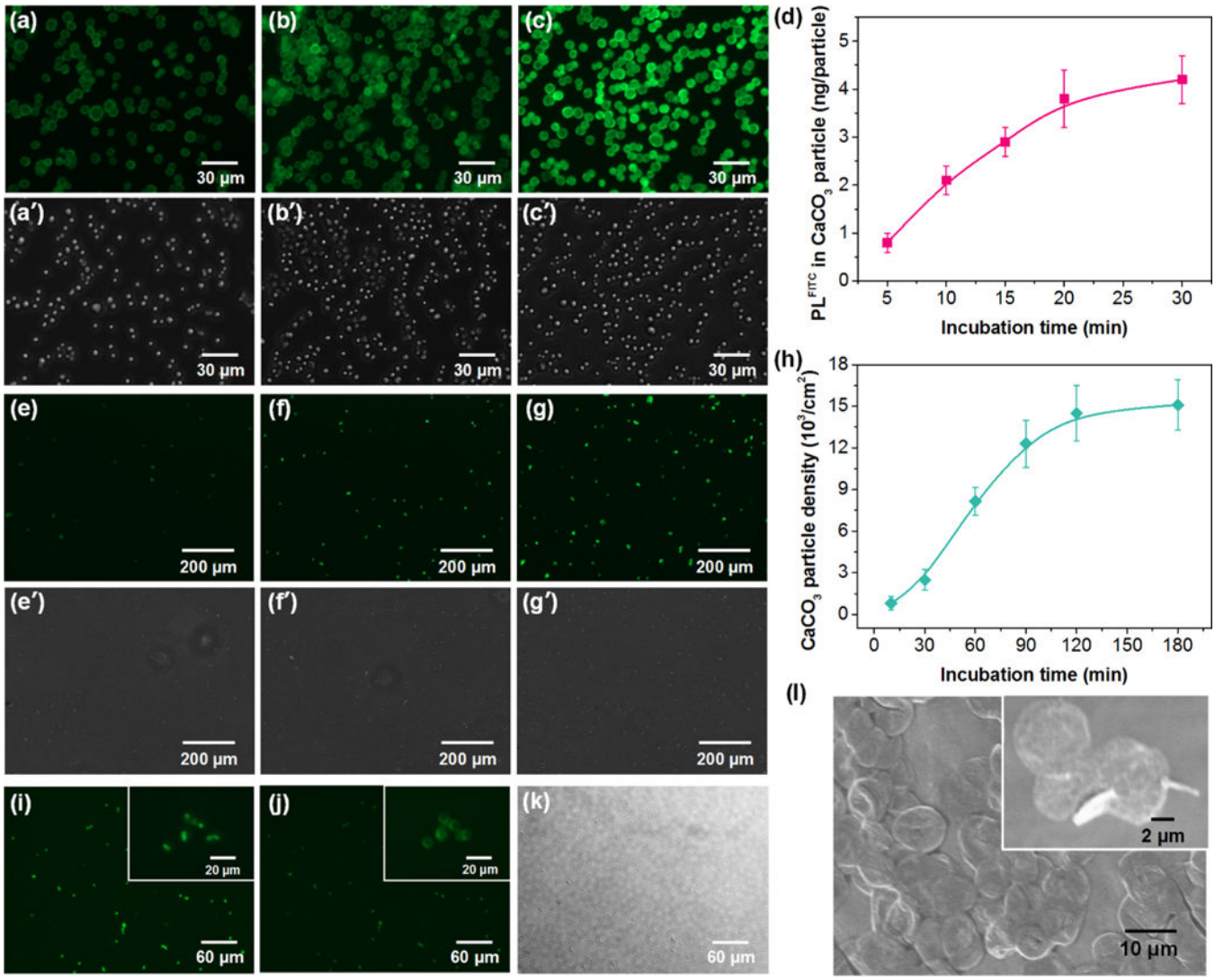

Figure 3.

CLSM images of $CaCO_3^{PL\text{-}FITC}$ particles with different incubation time of (a) 5, (b) 15, and (c) 30 min in PL-FITC solution, (a')-(c') are the corresponding images under transmittance mode. (d) Impregnation of PL within $CaCO_3$ particles as a function of incubation time in 2 mg mL^{-1} of PL solution. CLSM image of $CaCO_3^{PL\ FITC}$ particle assembled on multilayer films with different incubation time of (e) 30, (f) 60, and (g) 120 min in $CaCO_3$ $^{PL\text{-}FITC}$ particle suspension, (e')-(g') are the corresponding images under transmittance mode. (h) $CaCO_3$ particle density on $(PL/PG)_5$ multilayer films as a function of incubation time in $CaCO_3$ particle suspension (6×10^6 particles mL^{-1}). In situ observation of $(PL/\ PG)_5$/ capsule$^{PL\text{-}FITC}$/PG/$(PL/PG)_8$ films CLSM images (i) before and (j) after $CaCO_3$ decomposition under fluorescence mode and (k) is the corresponding image of (j) under transmittance mode. (l) SEM image of the $(PL/PG)_5$/capsule $^{PL\text{-}FITC}$ /PG/$(PL/PG)_8$ multilayer films.

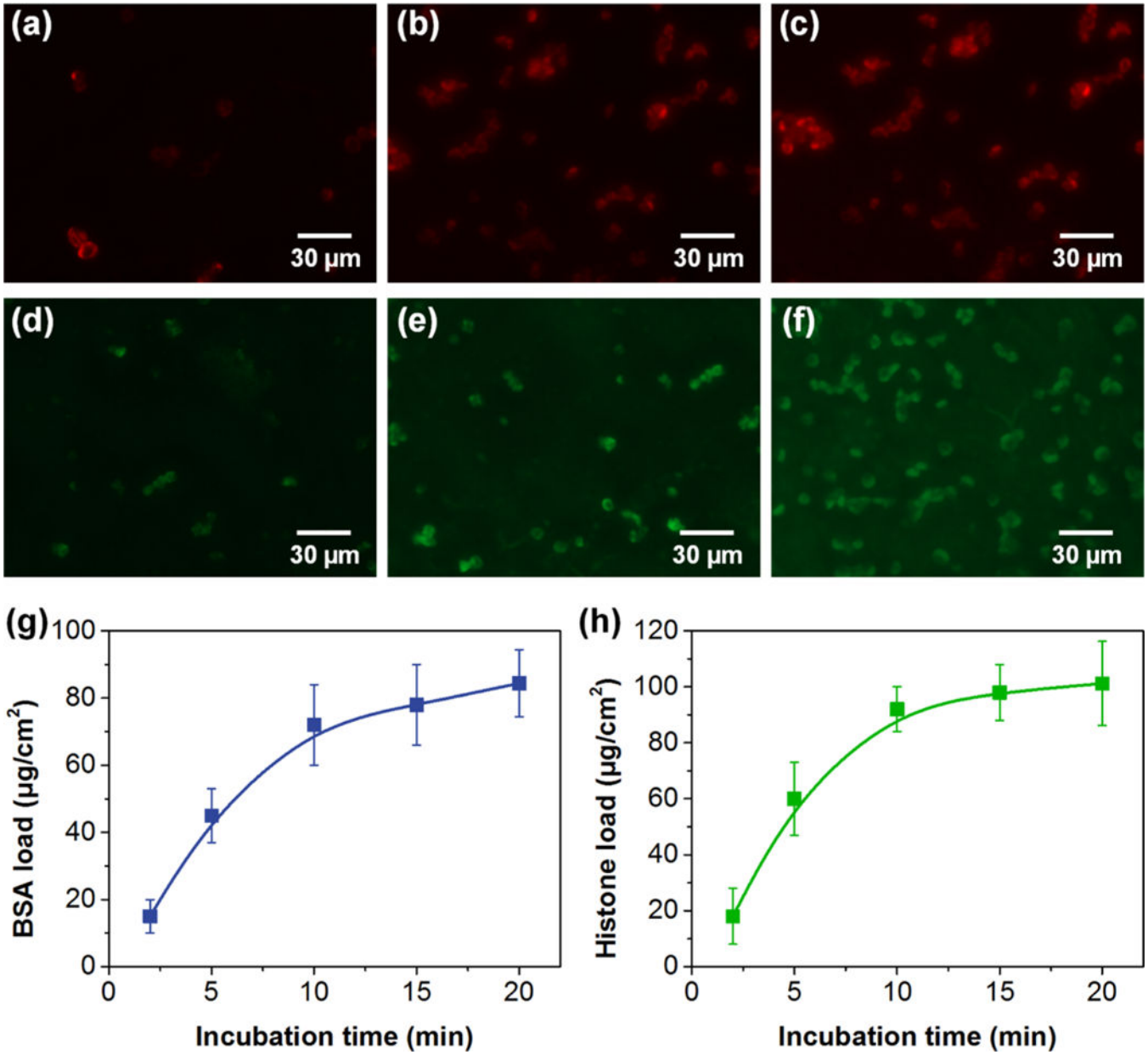

Figure 4.

CLSM images of delivery vehicles of $L_5/C^G/L_8/C^L/L_8$ films loaded with BSA for (a) 2, (b) 10, and (c) 20 min and loaded with histone for (d) 2, (e) 10, and (f) 20 min. Loading profiles of (g) BSA and (h) histone with increasing incubation time. BSA and histone are visualized at (a-c) 647 and (d-f) 488 nm, respectively.

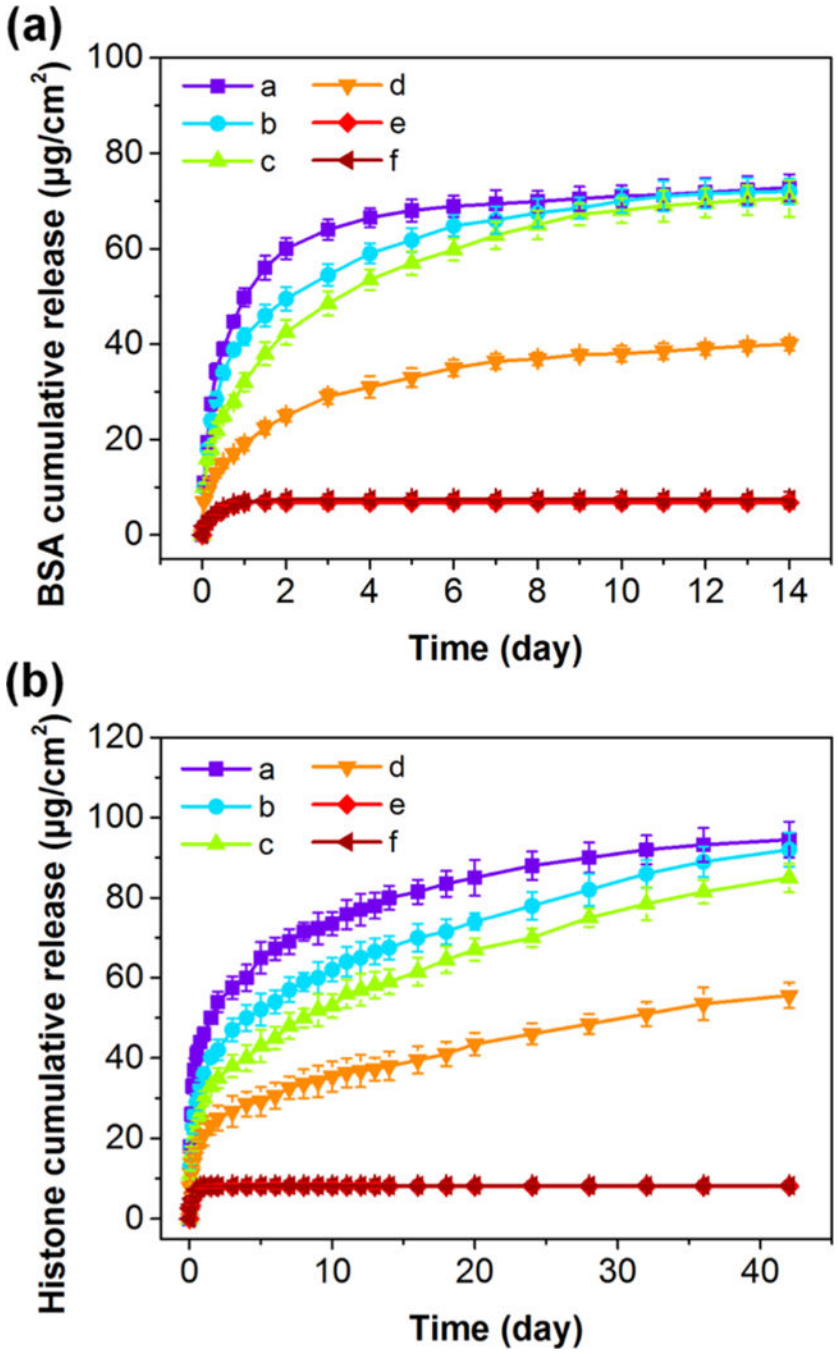

Figure 5.

Cumulative release profiles of (a) BSA and (b) histone from PL/PG multilayer films with and without capsule^{PL} or capsule^{PG} and with different loading incubation time. The samples used in (a) included (a) $L_5/C^G/L_8/C^L/L_3$ film, (b) $L_5/C^G/L_8/C^L/L_8$ film, (c) $L_5/C^G/L_8/C^L/L_{13}$ film, (d) $L_5/C^G/L_8/C^L/L_8$ film incubated in drug solutions for 5 min, (e) $L_5/C^G/L_8/C^G/Li$ film, and (f) L_{18} film. The samples used in (b) included (a) $L_5/C^G/L_3/C^L/L_8$ film, (b) $L_5/C^G/L_8/C^L/L_8$ film, (c) $L_5/C^G/L_{13}/C^l/L_8$ film, (d) $L_5/C^G/L_8/C^L/L_8$ film incubated in drug

solutions for 5 min, (e) $L_5/C^L/L_8/C^L/L/_8$ film, and (f) L_{18} film. All of the samples were incubated for 15 min unless otherwise noted.

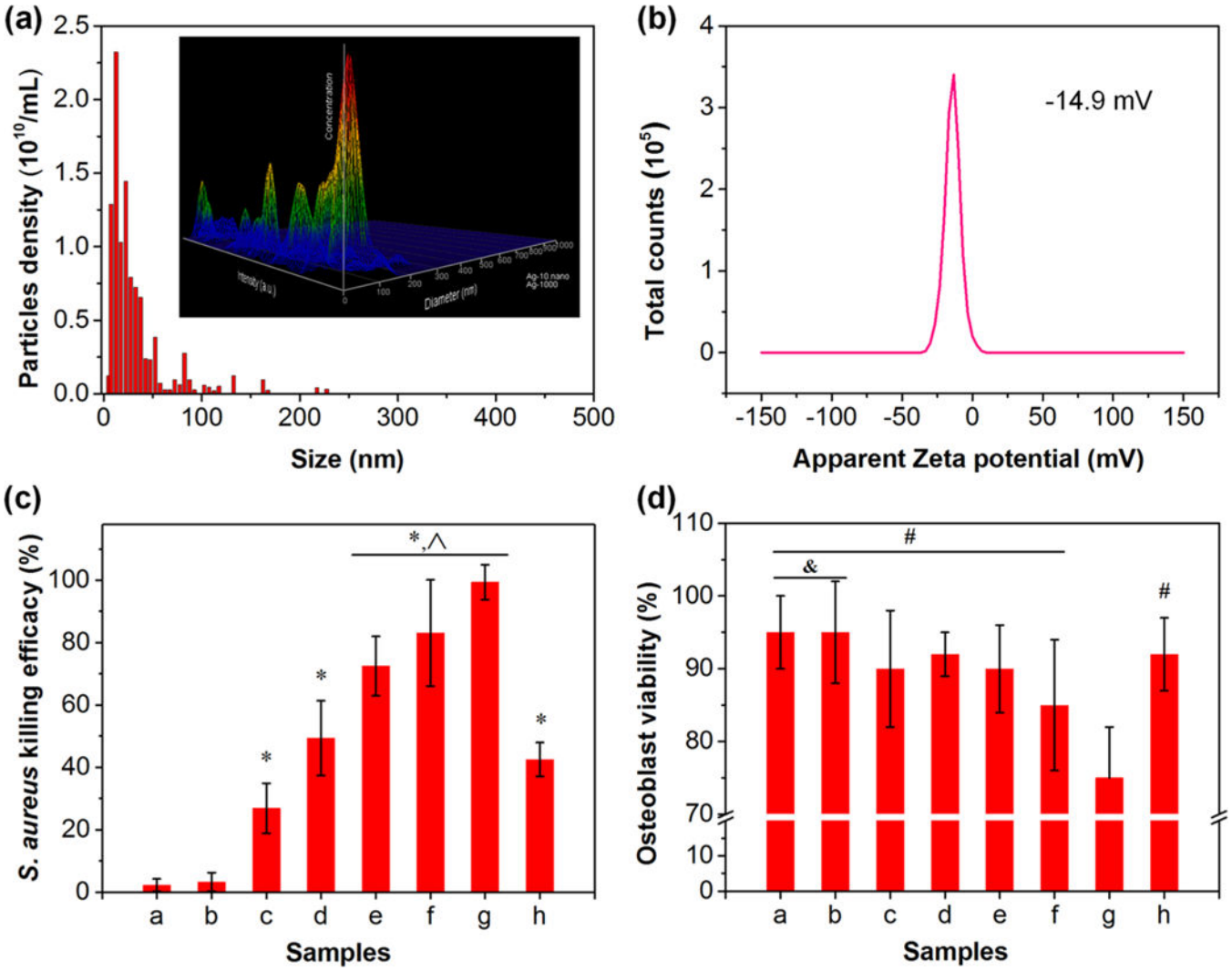

Figure 6.

(a) Size distribution and (b) ζ potential of PVP-capped AgNPs. Inset is the corresponding normalized 3D graph (size vs intensity vs concentration). (c) *S. aureus* killing efficacy and (d) osteoblast viability of various delivery vehicles with/without AgNP loading and AgNP suspensions. The samples used in (c) and (d) included (a) L_{23} film, (b) $L_5/C^G/L_8/C^L/L_8$ film, (c-f) $L_5/C^G/L_8/C^{L+AgNPs}/L_8$ film incubated in Ag suspension for 5, 20, 40, and 60 min, respectively, (g) 93 μM Ag suspension, and (h) 20 μM Ag suspension. * $p < 0.01$ compared to sample (a), $^{\wedge}$ $p < 0.01$ compared to sample (c). $^{\#}$ $p < 0.01$ compared to sample (g). $^{\&}$ $p < 0.01$ compared to sample (f).

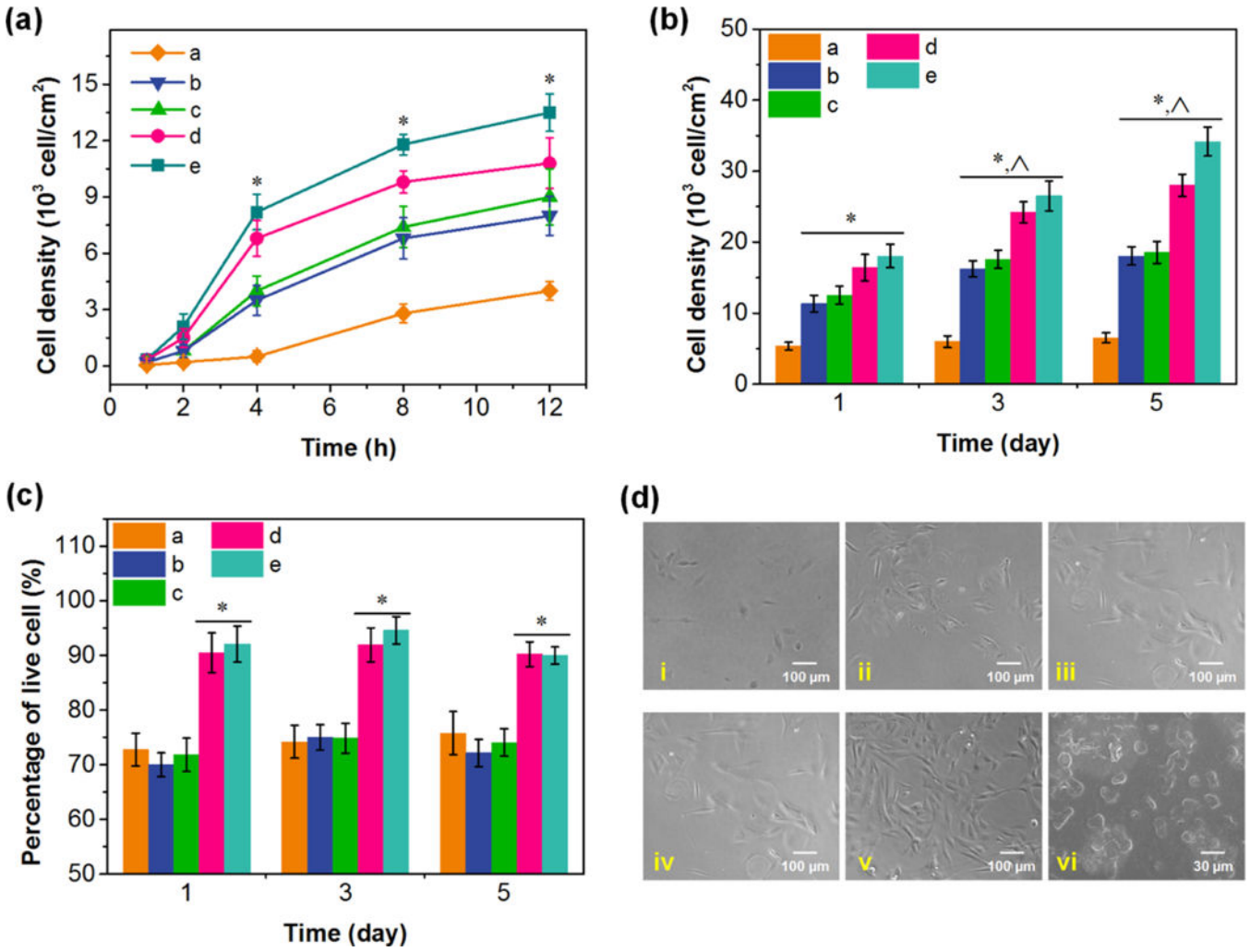

Figure 7.

(a) Cell density of osteoblast cells on control substrates, substrates with PL/PG multilayer film, and substrates with PL/PG films incorporated with rhBMP-2 at 1, 2, 4, 8, and 12 h. (b) Proliferation of osteoblast cells and (c) percentage of living cells on various substrates at 1, 3, and 5 days. The samples used in (a)-(c) included (a) quartz slide, (b) L_{23} film, (c) $L_5/C^G/L_8/C^L/L_8$ film, (d, e) $L_5/C^{G+BMP}/L_8/C^L/L_8$ films incubated in rhBMP-2 solution for 5 and 15 min, respectively. (d) Images of osteoblast cell adhesion on samples in (b) and (c) at 24 h. (i-v) Correspond to the samples (a)-(e), respectively. (vi) SEM image of osteoblast cell adhesion. * $p < 0.01$ compared to quartz, ^ $p < 0.01$ compared to the same samples cultured at 1 day.

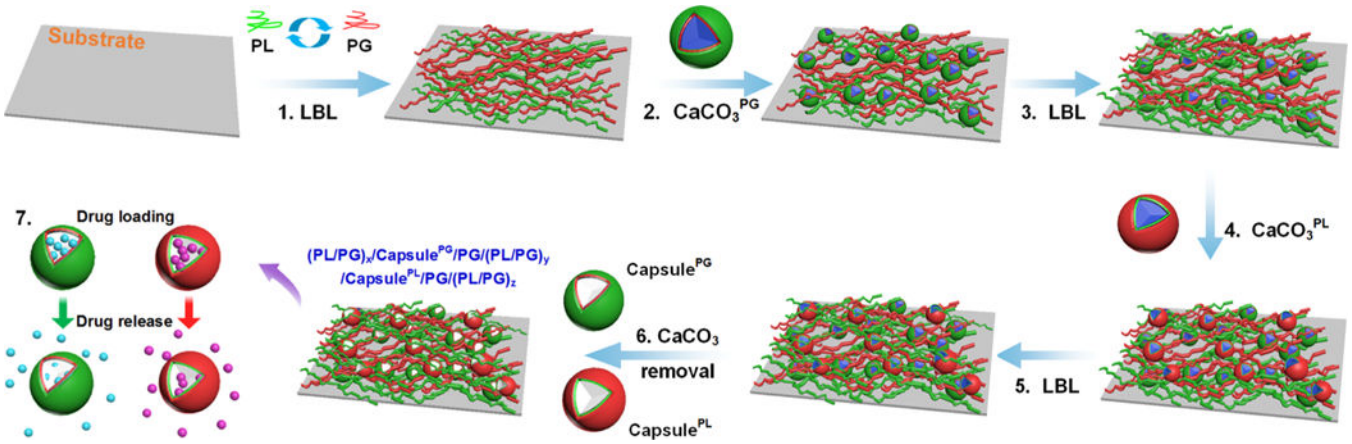

Scheme 1. Schematic Diagram Showing the Formation Process of Capsule-Integrated PL/PG Multilayer Films for Multidrug Delivery Using LbL Self-Assembly Technology[a]

[a]The capsules impregnated with PL or PG polypeptides can function as vehicles for positively and negatively charged drug loading and release. (1) Self-assembly of $(PL/PG)_X$ multilayer nanofilms; (2) deposition of PG-impregnated $CaCO_3$ particles ($CaCO_3^{PG}$); (3) self-assembly of $PG/(PL/PG)_Y$ multilayer nanofilms; (4) deposition of PL-impregnated $CaCO_3$ particles ($CaCO_3^{PL}$); (5) self-assembly of $PG/(PL/PG)_Z$ multilayer nanofilms; (6) formation of capsule-integrated multilayer films by dissolving $CaCO_3$ templates; and (7) pH-controlled drug loading and release.